Electronic Supplementary Material (ESI) for Energy & Environmental Science.

Supplementary Information

Multi-beam spark plasma sintering and excellent performance of $Bi_{0.5}Sb_{1.5}Te_3$/epoxy thermoelectric films with insulating substrate

Shaoqiu Ke[1], *Dong Liang*[1], *Xiaolei Nie**, *Xiaoling Ai*, *Longzhou Li*, *Chengshan Liu*, *Wenjie Xu*, *Wenjun Cui*, *Xianfeng Ye*, *Tiantian Chen*, *Xiangyu Li*, *Kai Fu*, *Wanting Zhu*, *Ping Wei*, *Wenyu Zhao**, and *Qingjie Zhang*

State Key Laboratory of Advanced Technology for Materials Synthesis and Processing, Wuhan University of Technology, Wuhan 430070, China

[1] These authors contributed equally to this work

* Corresponding authors: W. Zhao (wyzhao@whut.edu.cn) and X. Nie (xiaoleinie@whut.edu.cn)

S1. Preparation of $Bi_{0.5}Sb_{1.5}Te_{3.0}$/epoxy films

In this study, a series of *p*-type $Bi_{0.5}Sb_{1.5}Te_{3.0}$/epoxy (BST/EP) films with {000*l*} preferential orientation was prepared on insulating polyimide (PI) substrates by combining screen-printing and SPS techniques according to **SFig. 1**. Firstly, the BST/EP slurries were prepared and ultrasonically dispersed to make uniform, and the through-holes were made on the PI substrate by laser etching technology. Secondly, the BST/EP slurries were screen-printed onto the porous PI substrates, and then the films were engraved into circles with a diameter of 25 mm by laser etching technology after drying. Finally, the circular films were placed in SPS mould and sintered to yield compact BST/EP films, which was labeled as MB-BST/EP. To better compare the effect of substrates with or without through-holes on the properties of the BST/EP films, an extra sample of BST/EP film printed on PI substrates without through-holes was sintered by SPS at the same sintering conditions in this work, which was labeled as C-BST/EP.

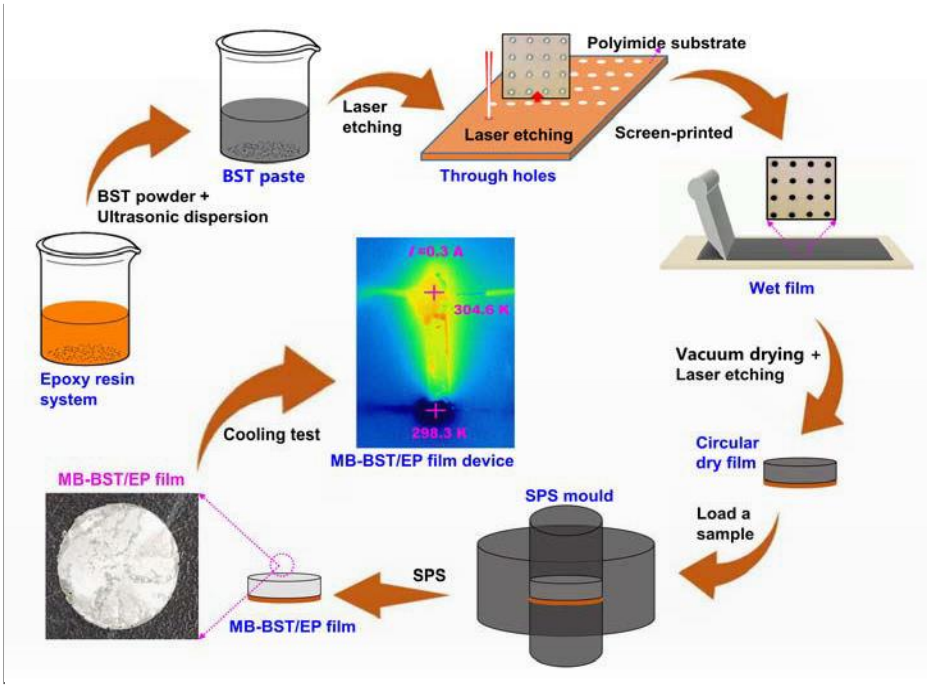

Supplementary Fig. 1. Schematic illustration of preparing BST/EP films.

S2. Transport measurement of BST/EP films

The orientation factors (*F*) of {000*l*} preferential orientation for all the BST/EP films were calculated with Lotgering's method[1]

$$F(X)=(P-P_0)/(1-P_0) \quad \text{(S1)}$$

$$P=\Sigma I(X)/\Sigma I(hkil) \qquad P_0=\Sigma I_0(X)/\Sigma I_0(hkil) \quad \text{(S2)}$$

where $\Sigma I(X)$, $\Sigma I_0(X)$, $\Sigma I(hkil)$, and $\Sigma I_0(hkil)$ are the sums of the intensities of the X and ($hkil$) reflections for the oriented sample and the non-oriented one, respectively; P and P_0 are the ratios of the sums for the oriented sample and the non-oriented one, respectively.

The thickness of the BST/EP films were obtained from backscattered electron images by EPMA. The detailed samples preparation and testing methods were shown in **SFig. 2**. The samples preparation for EPMA was shown in **SFig. 2a**. Firstly, the BST/EP films were secured to the microscope cover glass by double-sided tape. Secondly, the cold mounting agent was mixed evenly, and the cold mounting agent was composed of 2 g powdered epoxy resin and 1.6 g liquid curing agent. Thirdly, the evenly cold mounting agent were poured into the silicone plastic cold mounting mold with an inner diameter of 20 mm, then the microscope cover glass was vertically placed with the BST/EP films into the cold mounting mold with cold mounting agent, the microscope cover glass was secured by toothpicks, and then let the cold mounting mold stand at room temperature for 2 h to wait for the cold mounting agent to cure. Lastly, the mounted samples were obtained by stripping the cold mounting mold, and the mounted samples were polished to obtain the samples for EPMA.

To obtain the thickness of the BST/EP films more accurately, the samples for EPMA was sprayed with a layer of carbon about 15 nm before the test. The thickness of MB-BST/EP film was obtained from EPMA by using backscattered electron images as shown in **SFig. 2b-c**. The gray-white contrast was BST as shown in **SFig. 2b**. It could be clearly seen that part of the BST in the MB-BST/EP film had entered the through hole of the PI substrate, and the distance between the right edge of the through hole and the left edge of the next through hole was about 1167 μm. The thickness of each part of the MB-BST/EP film cross-section were 100 μm, 108 μm, 120 μm, 125 μm, 130 μm, 120 μm, 120 μm, 120 μm, 123 μm, 128 μm, 130 μm, 135 μm, and 138 μm, respectively. It could also be clearly seen that the thickness of MB-BST/EP film near the through-hole were 135 μm and 140 μm, respectively, the thickness of BST including the through-hole thickness was about 244 μm, and the width of the through-hole was about 343 μm as shown in **SFig. 2c**. The weighted average thickness of the MB-BST/EP film was about 139.38 μm by counting the thickness of each part of the MB-BST/EP film cross-section, including the through-hole thickness data and the non-through hole thickness data. Therefore, the thickness data used in the measurement of the electrical and thermal transport properties of the BST/EP

films was 139 μm. Moreover, the BST contact of the cross-section of the MB-BST/EP film was closed as shown in **SFig. 2c**, and there were almost no pores in the cross-section of the MB-BST/EP film, which is beneficial to the excellent electrical transport properties.

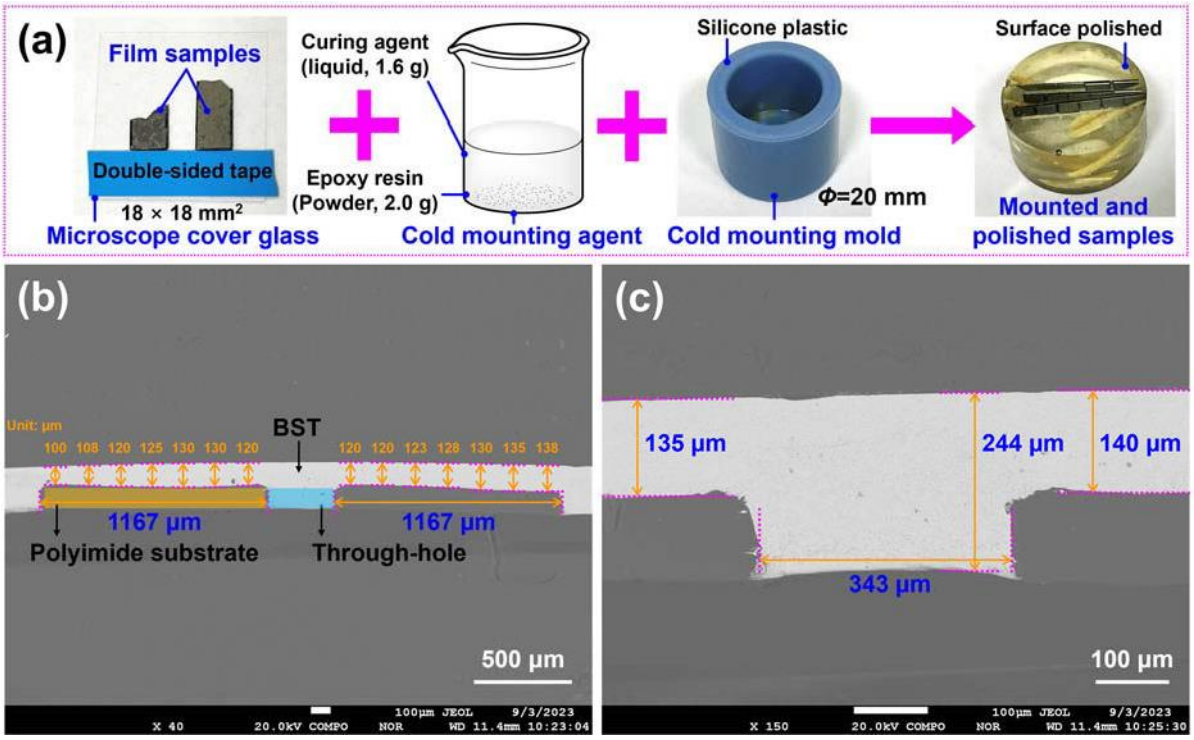

Supplementary Fig. 2 The samples preparation for EPMA and microstructures of MB-BST/EP film from EPMA. (**a**) The samples preparation for EPMA. (**b**) Backscattered electron images of a polished cross section of the MB-BST/EP film and (**c**) the magnification backscattered electron images of a polished cross section of the MB-BST/EP film obtained by EPMA.

To figure out the reasons for the changes in electrical transport properties induced by MB-SPS, traditional van der Pauw Hall measurement method was performed. Firstly, the slopes k_H of C-BST/EP film and MB-BST/EP film were measured at 300 K with the Van der Pauw method under a fixed current (i =10 mA) at 1.0 Tesla (T). Secondly, the R_H of all the samples were calculated with the formula $R_H = k_H d/(i\mu_0)$, where d is the thickness of samples and μ_0 is the vacuum permeability ($\mu_0 = 4\pi\times10^{-7}$ V·s·A^{-1}·m^{-1}). Lastly, the carrier concentration (p) and carrier mobility (μ) were calculated according to the equations $p = 1/(eR_H)$ and $\mu=\sigma R_H$, where e is the electron charge (e =1.6 × 10^{-19} C), σ is electrical conductivity.

The Seebeck coefficient (α) and electrical conductivity (σ) were measured simultaneously using a standard four-probe method (CTA-3, Beijing Cryoall Science and Technology Co., Ltd., Beijing, China) in helium atmosphere from 300 K to 500 K. The principle of the standard four-probe test method and the test details of CTA-3 were shown in **SFig. 3**. The test accessories of CTA-3 for film sample was shown in **SFig. 3a**. The fixture consists of

two 316 stainless steel chucks and a silicon chip. The film sample with size of 3.8×14.0×0.139 mm^3 is placed on the silicon chip with size of 4.0×14.0 mm^2, and both ends of the film sample are clamped with a chuck. The assembled film sample is shown in **SFig. 3b**. Then the assembled film is put into the test system (the inset in **SFig. 3c**). The physical image after correctly placing the sample is shown in **SFig. 3d**. The fixture can ensure the 0.06 mm films be measured reliably with such a system. The detail test procedure and principle are as follows.

The assembled film sample is placed vertically between the upper and lower electrodes. The constant current I is applied at both ends of the sample as the overall temperature of the sample is evenly distributed. The voltage V is recorded at the same time as shown in **SFig. 3c**. If the spacing of the lateral probe is L and the horizontal cross section of the test sample is S, the σ of the material can be calculated by $\sigma = IL/VS$. Unlike σ tests of other materials, the σ test of thermoelectric materials will be inaccurate since the Seebeck effect will produce a more obvious additional voltage, so it will be tested three times to eliminate the error caused by the additional effect. The low end of the sample will be heated by the secondary heater, and the voltage difference (ΔV) and temperature difference (ΔT) between the two contact points with be detected by the two contact points. The α of the sample can be calculated according to the definition $\alpha = \Delta V/\Delta T$. Uncertainties are ± 5-7% for σ and about ± 5% for α.

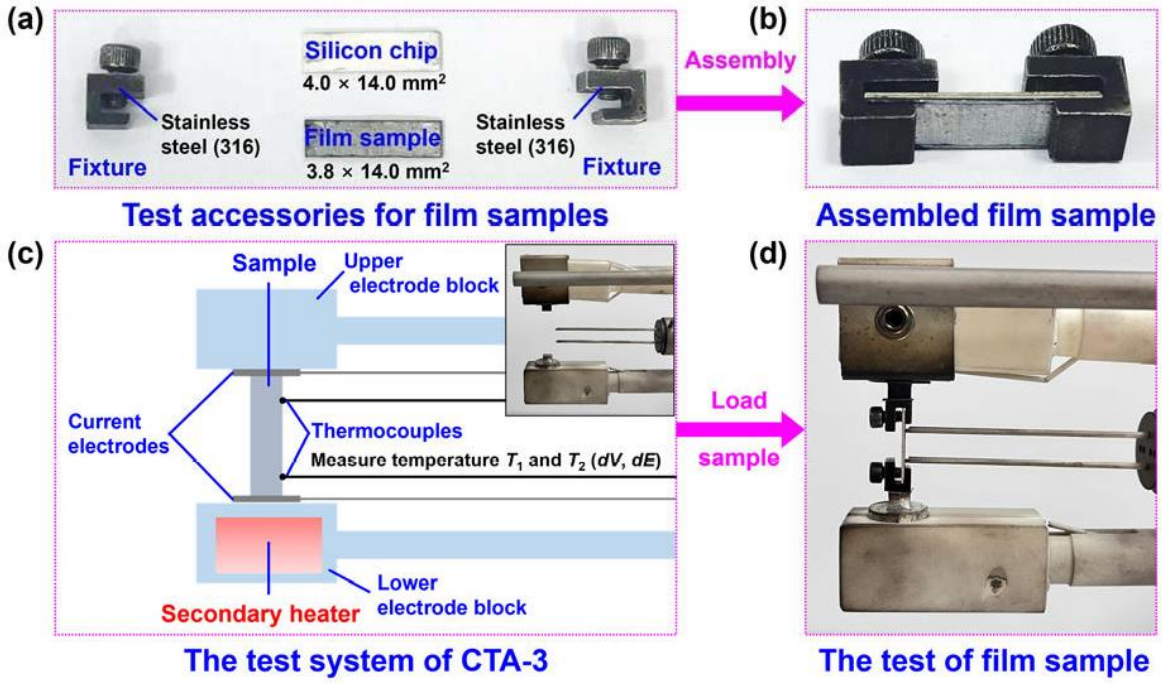

Supplementary Fig. 3 The test schematic of the electrical transport performance of the all BST/EP films. (**a**) The test accessories for film samples. (**b**) The image of assembled film sample. (**c**) The sketch map of CTA-3 measurement system. (**d**) The actual test image of film sample. The inset in (**c**) show the actual test system of CTA-3.

To explore the degree of uniformity of the microstructure and electrical transport performance of BST/EP films, three areas with the same size (3.8×14.0 mm) were etched by laser from the edge to the center of C-BST/EP film and MB-BST/EP film with diameters of 25 mm as shown in **SFig. 4a**, respectively. The electrical transport properties were tested by CTA-3. The MB-BST/EP film have a worth record power factor (*PF*) $\alpha^2\sigma$ of 2.47 at 300 K as shown in **SFig. 5**, which is more than all the room-temperature $\alpha^2\sigma$ values of TE films reported by different groups.

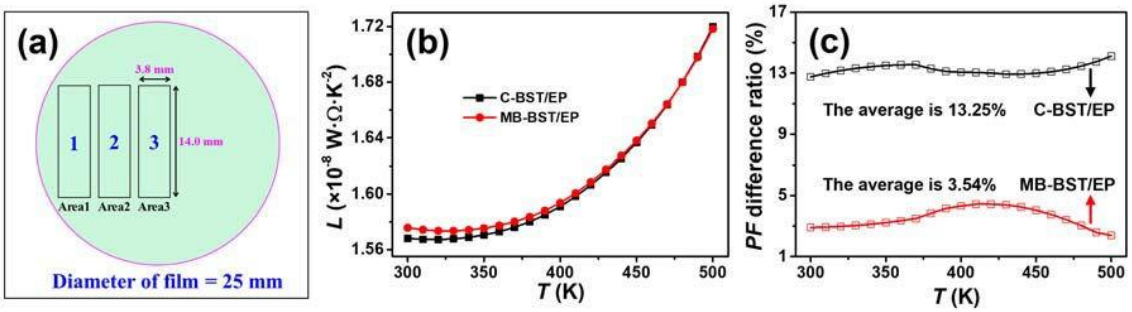

Supplementary Fig. 4 The electrical transport properties of the C-BST/EP film and MB-BST/EP film. (**a**) Schematic diagram of the sampling methods; The temperature dependence of (**b**) Lorentz number *L*, where the *L* was used to calculate the carrier thermal conductivity κ_C from the Wiedemann-Franz law $\kappa_C=L\sigma T$; (**c**) The power factor (*PF*) difference ratio of the C-BST/EP film and MB-BST/EP film.

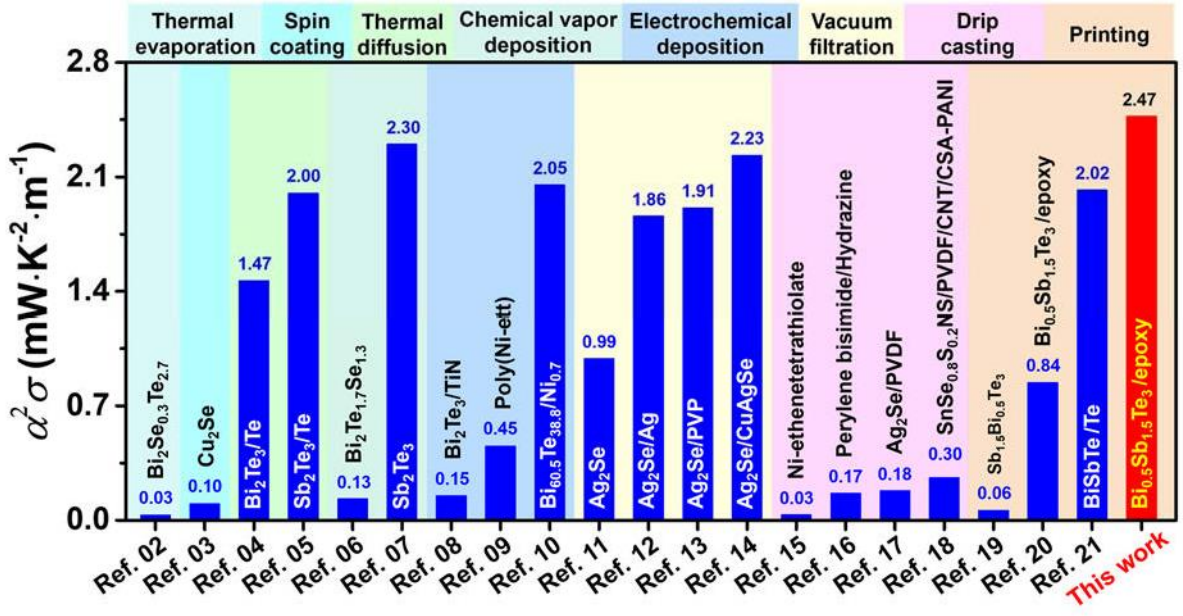

Supplementary Fig. 5 The room temperature *PF* values of TE films from different groups[2-21]

The in-plane thermal conductivity κ of all the MFEs/BST/epoxy flexible films was calculated with the formula $\kappa=\rho\cdot D\cdot C_p$, where ρ is the density, D is the in-plane thermal diffusivity, and C_p is specific heat capacity. The in-plane thermal diffusivity D was measured by a laser flash method (LFA467, NETZSCH). The in-plane D of

samples composed with very thin TE films and substrates will be seriously affected by the substrates because it is hardly to separate the TE films from the substrates without destroying the TE films. There are some differences between the BST/EP films and polyimide (PI) substrates. Therefore, our samples with about *Φ* 22 mm for measuring the in-plane *D* are free-standing BST/EP films with about 220 μm in thickness, which were prepared by repeatedly screen-printing until 8 times and then exfoliated the PI substrates with low *D*. Although the *D* of thick films are usually higher than those of thin films, our method can successfully avoid the problem of overestimating the *zT* value of thin films in some published papers. At the same time, to further evaluate the *D* and *zT* value of the BST/EP films more accurately, the in-plane *D* of a polished surface BST/EP film with about 139 μm in thickness and the PI substrate was also tested.

The measuring mold for the out-of-plane *D* and the in-plane *D* was shown in **SFig. 6a-b**. The out-of-plane *D* test method and principle of the laser flash method are as follows: the sample with a thickness of *L* is placed on the sample holder, and after reaching stability at a certain set temperature *T*, a laser pulse is emitted to the lower surface of the sample, and the temperature of the lower surface rises instantaneously. Under the action of temperature gradient, the heat energy diffuses from the lower table of the sample to the upper surface, the temperature change on the upper surface of the sample can be detected by the infrared detector as shown in **SFig. 6c**, and the corresponding signal intensity change curve over time *t* is obtained. The out-of-plane *D* of sample is determined by the parker-formula[22] ($D= 0.1388\times L^2/t_{0.5}$, where *L* is the thickness of the test sample, $t_{0.5}$ is the time required for the upper surface to reach half of the maximum temperature rise.). Different from measuring the out-of-plane *D* (**SFig. 6c**), during the measuring of the in-plane *D*, the bottom of the sample first receives laser pulse irradiation (a circle about 5 mm in the center), and then the sample temperature signal reaches the detector through the four-ring at the mask, and lastly the temperature signal along the in-plane direction is measured (**SFig. 6d**) and the in-plane *D* is obtained with the measurement error about 5%. For different film materials, the different calculation models need to be chosen. For BST/EP films with the anisotropic texture, after the center of the lower surface of the sample is irradiated, the heat will transfer to the horizontal and vertical directions at the same time, to obtain accurate test result of the in-plane *D*, the vertical *D* needs to be corrected as follows: 1) Measuring the in-plane and out-of-plane *D* of the film sample by placing one film sample with about *Φ* 22 mm on the in-plane measuring setup as shown in **SFig. 6d**, and another film sample with about *Φ* 12.7 mm on the out-of-plane measuring setup as shown in **SFig. 6c**; 2) Saving the *D* in the vertical direction in the analysis software. According to the "Anisotropy" model, in which the *D* from the *z*-axis (out-of-plane) differs compared to the *D* in the *x*/*y*-plane (in-plane), the solution is given as the product of two components, axial and radial, as expressed in the following formula:[23]

$$\theta(x^*,t^*) = \theta_x(x^*,t^*) \cdot \theta_r(t^*)$$

$$\theta_x(x^*,t^*) = 2\sum_{n=1}^{\infty} \frac{\beta_n \cos(\beta_n x^*) + Bi_0 \sin(\beta_n x^*)}{(\beta_n^2 + Bi_0^2 + Bi_0)\left[1 + Bi_L/(\beta_n^2 + Bi_L^2)\right] + Bi_0} \exp(-\beta_n^2 t^*)$$

$$\theta_r(t^*) = 2\sum_{p=1}^{\infty} \frac{\gamma_p}{J_0(\gamma_p)\sqrt{(Bi_R R)^2 + \gamma_p^2}} \cdot \zeta_0 J_1(\zeta_0 \gamma_p) \frac{2\left[J_0(\gamma_p R_0) - R_0 J_1(\gamma_p R_0)\right]}{\gamma_p (R_0^2 - R_I^2)} \exp(-\gamma_p^2 t^*)$$

$$R_I = \frac{R_I}{L} \qquad R_0 = R_0/L$$

All the mathematical parameters used in the "Anisotropy" model are listed in **STable 1**. According to the measured results of in-plane ($\theta(x^*,t^*)$) and out-of-plane ($\theta_x(x^*,t^*)$), the accurate in-plane D k ($\theta_r(t^*)$) of BST/EP films can be obtained. The system error of the measurement mainly depends on the thermal property and thickness of the film. The lower the thermal conductivity of the film is, the greater the measurement error is; and the thicker the film is, the smaller the measurement error is. Therefore, to obtain accurate in-plane D, the out-of-plane thermal transfer needs to be corrected.

STable 1 All the mathematical parameters used in the "Anisotropy" model

Short cut	Description
D	Thermal diffusivity
[?]	Thermal conductivity
[?]	Sample′s thickness
R	Sample′s radius
[?] [?] = (h [?])/[?]	Corresponding Biot number
ζ_0	Beam ratio
ζ_L	Detection area
J	Sensitivity matric
β	Positive roots of (transcendental equation): $\tan(\beta) = \frac{\beta(Bi_0 + Bi_L)}{\beta^2 - Bi_0 Bi_L}$
γ	Positive roots of (transcendental equation): $\gamma \cdot J_1(\gamma) = Bi_R R^* J_0(\gamma)$
$x^*=x/L$	Dimensionless parameter
$R^0=R/L$	Dimensionless parameter
$t^*=\alpha \cdot t/L^2$	Dimensionless parameter

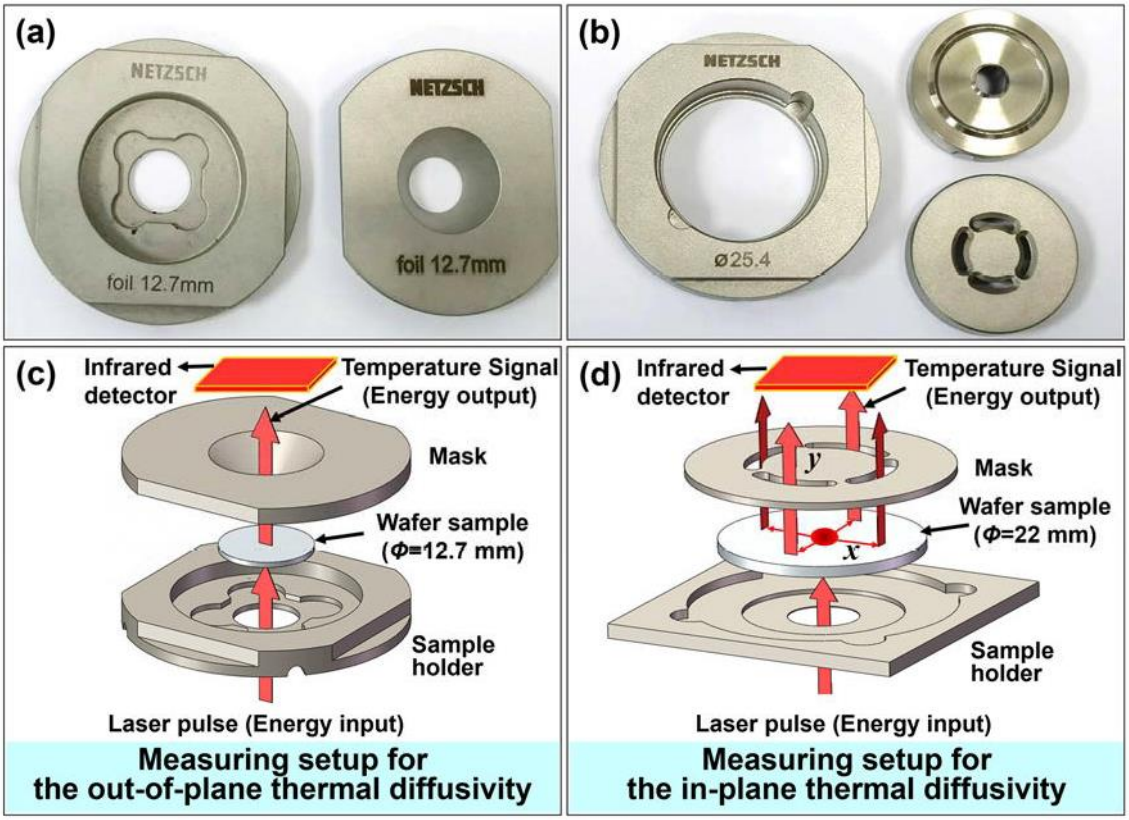

Supplementary Fig. 6 Schematic plot for measuring the in-plain thermal diffusivity *D* of all the BST/EP films. The actual measuring mold figure for (**a**) the out-plane *D* and (**b**) the in-plane *D*. The measuring setup for (**d**) the out-of-plane *D* and (**e**) the in-plane *D*.

The details of room temperature thermal property of free-standing C-BST/EP film and MB-BST/EP film without insulating PI substrates are listed in **STable 2**. The details of room temperature thermal property of the C-BST/EP film and MB-BST/EP film with insulating PI substrates are listed in **STable 3**. To further evaluate the *D* and *ZT* value of the BST/EP films more accurately, the in-plane *D* of a polished surface BST/EP film with thickness about 139 μm and the PI substrate was also tested. The temperature dependence of the in-plane thermal conductivity κ, carrier thermal conductivity κ_C, lattice thermal conductivity κ_L, and *ZT* of C-BST/EP film and MB-BST/EP film with PI substrate were shown in **SFig. 7**, respectively. The κ of all samples first decreases and then increases with increasing temperature as shown in **SFig. 7a**. The decrease in κ is due to the increase of lattice vibration, and the increase in the κ is due to intrinsic excitation. The κ_C of all samples increases with increasing temperature due to the increased σ of all samples as shown in **SFig. 7b**. The κ_C of the MB-BST/EP film is significantly higher compared with that of the C-BST/EP film. This is attributed to the remarkable increase of σ of MB-BST/EP film (**Fig. 5a**). The κ_L of all samples was calculated by the $\kappa_L = \kappa - \kappa_C$. The κ_L shows the same trend as κ with increasing temperature because the contribution of κ_C to κ is small as shown in **SFig. 7c**. The κ of the MB-BST/EP film is significantly lower compared with that of the C-BST/EP film as shown in **SFig. 7a**. The decrease of the κ is

attributed to the remarkable decrease of the κ_L induced by MB-SPS (**SFig. 7c**). The decrease of the κ_L is attributed to the increase of the DL stacking faults induced by MB-SPS (**Fig. 4b**). The calculated *zT* values, based on these measured σ, κ and α of area3, increased induced by MB-SPS (**SFig. 7d**). The maximum *zT* is about 1.38 at 340 K for MB-BST/EP film with PI substrate, increased by 2.0 times as compared with that of the C-BST/EP film with PI substrate, which is more than all the *zT* values of organic/inorganic composite TE films reported by different groups as shown in **SFig. 8**.

STable 2 The room temperature thermal properties of free-standing the C-BST/EP film and MB-BST/EP film without insulating PI substrates.

Samples	Density ρ ($g \cdot cm^{-3}$)	Specific heat capacity C_p ($J\ g^{-1}\ K^{-1}$)	Thermal diffusivity D ($mm^2\ s^{-1}$)	Thermal conductivity k ($W\ m^{-1}\ K^{-1}$)	zT
C-BST/EP	6.0300	0.2479	0.7103	1.0620	0.44
MB-BST/EP	6.3105	0.2708	0.5376	0.9188	0.81

STable 3 The room temperature thermal properties of the C-BST/EP film and MB-BST/EP film with insulating PI substrates.

Samples	Density ρ ($g \cdot cm^{-3}$)	Specific heat capacity C_p ($J\ g^{-1}\ K^{-1}$)	Thermal diffusivity D ($mm^2\ s^{-1}$)	Thermal conductivity k ($W\ m^{-1}\ K^{-1}$)	zT
C-BST/EP	6.0300	0.2479	0.5204	0.7780	0.59
MB-BST/EP	6.3105	0.2708	0.3698	0.6320	1.17

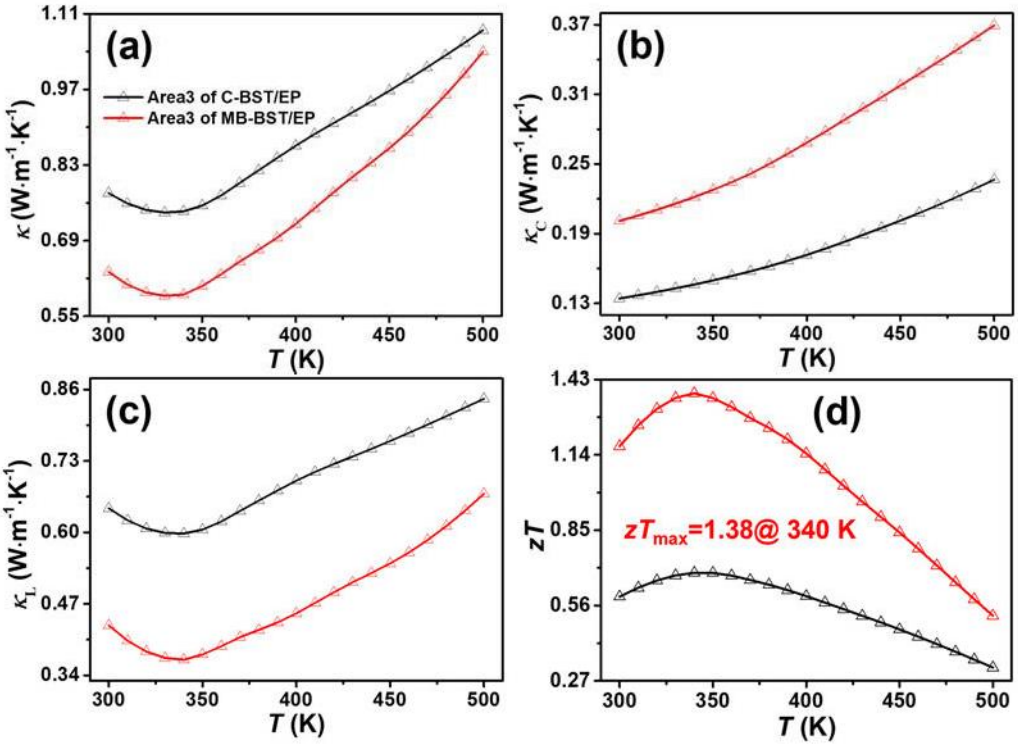

Supplementary Fig. 7 Thermal transport properties and *zT* of C-BST/EP film and MB-BST/EP film with PI substrate. Temperature dependence of (**a**) thermal conductivity κ, (**b**) carrier thermal conductivity κ_C, (**c**) lattice thermal conductivity κ_L, and (**d**) *zT* of the BST/EP films with PI substrate at same area.

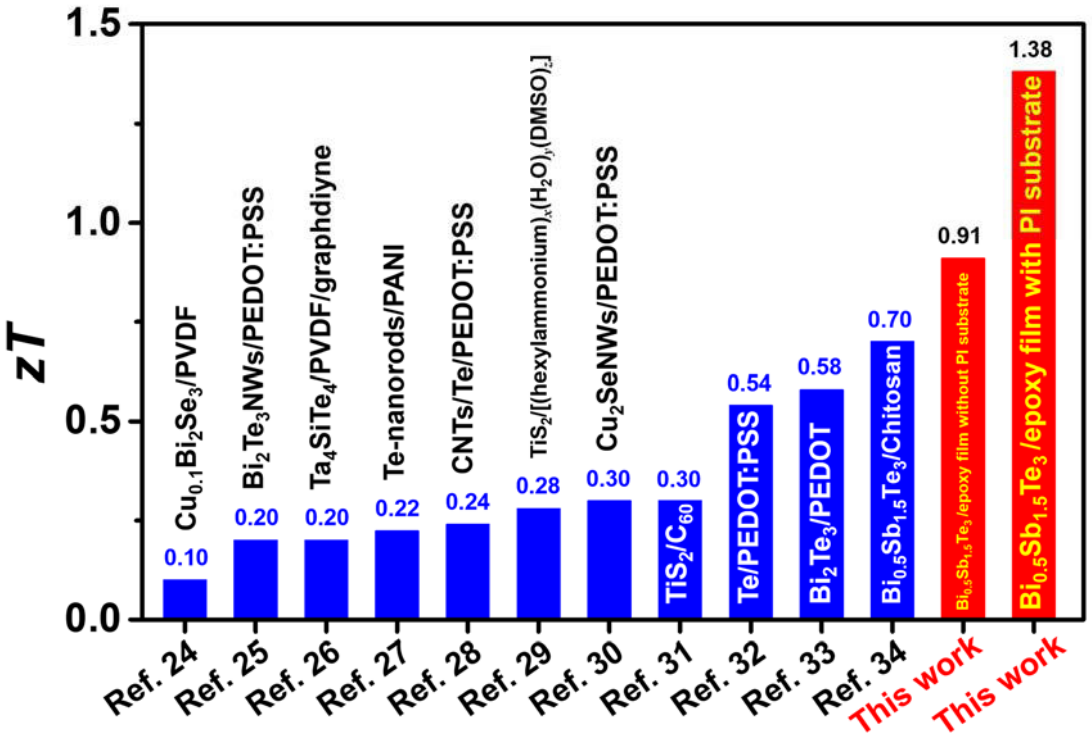

Supplementary Fig. 8 The maximum *zT* values of organic/inorganic composite TE films from different groups[24-34]

S3. Effect of uniaxial stress

A series of MB-BST/EP films are prepared under different uniaxial stress of 10 MPa, 15 MPa, 20 MPa, 25 MPa, and 30 MPa. The temperature dependence of σ, Seebeck coefficient α and $\alpha^2\sigma$ of MB-BST/EP films are shown in **SFig. 9a-c**, respectively. The σ of all samples first decreases and then increases as the temperature increases, exhibiting a typical metal-like nature or degenerate semiconductor behavior, and it gradually increases due to intrinsic excitation.[35] The σ first gradually increases and then decreases as uniaxial stress increases. The maximum σ reaches 4.39×10^4 S·m^{-1} at 300 K for the MB-BST/EP film under a uniaxial stress of 20 MPa, increased by 1.8 times compared with that of the MB-BST/EP film under a uniaxial stress of 10 MPa. The magnitude of α of MB-BST/EP films gradually decreases with temperature as shown in **SFig. 9b**. The decrease of α in the high temperature range is due to the intrinsic excitation.[35] Regardless of the temperature, the magnitude of α is almost unchanged as the uniaxial stress increases. The $\alpha^2\sigma$ values of all the MB-BST/EP films are calculated as shown in **SFig. 9c**. The $\alpha^2\sigma$ values of all samples decrease with increasing temperature. At the same time, the $\alpha^2\sigma$ values first increase and then decrease as uniaxial stress increases. The maximum $\alpha^2\sigma$ value reaches 2.50 mW·K^{-2}·m^{-1} at 300 K for the MB-BST/EP film under a uniaxial stress of 20 MPa, increased by 83% compared with that of the MB-BST/EP film under a uniaxial stress of 10 MPa. As a result, the optimum uniaxial stress for the MB-BST/EP films preparation is 20 MPa.

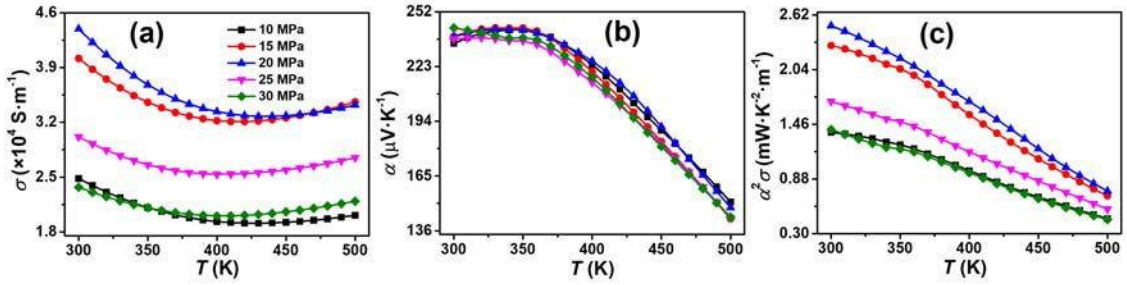

Supplementary Fig. 9 Electrical properties of MB-BST/EP films under different uniaxial stress.

Temperature dependence of (**a**) electrical conductivity, (**b**) Seebeck coefficient, and (**c**) *PF* of the MB-BST/EP films under different uniaxial stress.

S4. Effect of holding time

The effect of holding time during MB-SPS was investigated while keeping the heating rate of 9 K/min, peak sintering temperature of 573 K, and uniaxial pressure of 20 MPa. The temperature dependence of σ, α and $\alpha^2\sigma$ of MB-BST/EP films under different holding time are shown in **SFig. 10a-c**, respectively. The σ first gradually increases and then decreases as the holding time increases. The maximum σ reaches 4.39×10^4 S·m^{-1} at 300 K for

MB-BST/EP film under a holding time of 10 min, increased by 1.6 times compared with that of MB-BST/EP film under a holding time of 5 min. The remarkable increases of the σ for the MB-BST/EP film under a holding time of 10 min are attributed to the grain growth and re-orientation induced by the holding time increases.[36, 37] The remarkable decreases of the σ for the MB-BST/EP film under a holding time of 15 min are attributed to the slip and fracture of the layered BST particles induced by the longer holding time.[38] The magnitude of α of MB-BST/EP films under different holding time are shown in **SFig. 10b**. Regardless of the temperature, the magnitude of α first gradually slightly increases and then slightly decreases as the holding time increases. The maximum α at 300 K for MB-BST/EP film is realized under a holding time of 10 min. The $\alpha^2\sigma$ values of all the MB-BST/EP films under different holding time are calculated as shown in **SFig. 10c**. The $\alpha^2\sigma$ values first increase and then decrease as holding time increases. The maximum $\alpha^2\sigma$ of MB-BST/EP film under a holding time of 10 min. As a result, the optimum holding time for the MB-BST/EP films preparation is 10 min.

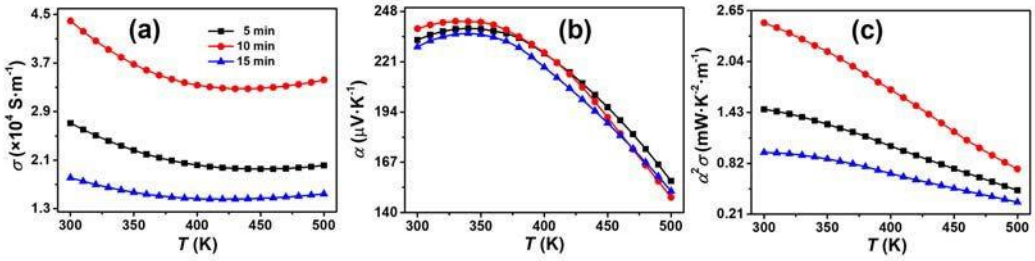

Supplementary Fig. 10 Electrical properties of MB-BST/EP films under different holding time.

Temperature dependence of (**a**) electrical conductivity, (**b**) Seebeck coefficient, and (**c**) *PF* of the MB-BST/EP films under different holding time.

S5. Effect of peak sintering temperature

The effect of peak sintering temperature during MB-SPS was investigated while keeping the heating rate of 9 K/min, holding time of 10 min, and uniaxial pressure of 20 MPa. The temperature dependence of σ, α and $\alpha^2\sigma$ of MB-BST/EP films under different peak sintering temperature is shown in **SFig. 11a-c**, respectively. The σ first gradually increases and then decreases as the peak sintering temperature increases. The maximum σ at 300 K for MB-BST/EP film is realized under peak sintering temperature of 573 K, increased by 1.4 times compared with that of MB-BST/EP film under peak sintering temperature of 553 K. The remarkable increases of the σ for the MB-BST/EP film under peak sintering temperature of 573 K are attributed to the grain growth and re-orientation induced by the higher peak sintering temperature.[36, 37] The remarkable decreases of the σ for the MB-BST/EP film under peak sintering temperature of 593 K are attributed to lower p induced by the rapidly increasing defect of anionic vacancy $V_{Te}^{\cdot\cdot}$ and e' induced by the donor-like effect from the higher peak sintering temperature.[39] The

magnitude of α of MB-BST/EP films under different peak sintering temperature are shown in **SFig. 11b**. Regardless of the temperature, the magnitude of α gradually increases as the peak sintering temperature increases. The increases of the α for the MB-BST/EP film are attributed to lower p. The $\alpha^2\sigma$ values of all the MB-BST/EP films under different peak sintering temperature are calculated as shown in **SFig. 11c**. The $\alpha^2\sigma$ values first increase and then decrease as peak sintering temperature increases, and the $\alpha^2\sigma$ values of BST/EP films are similar under 573 K and 593 K, but the BST/EP film is easily broken under 593 K. Therefore, the optimum peak sintering temperature for the MB-BST/EP films preparation is 573 K.

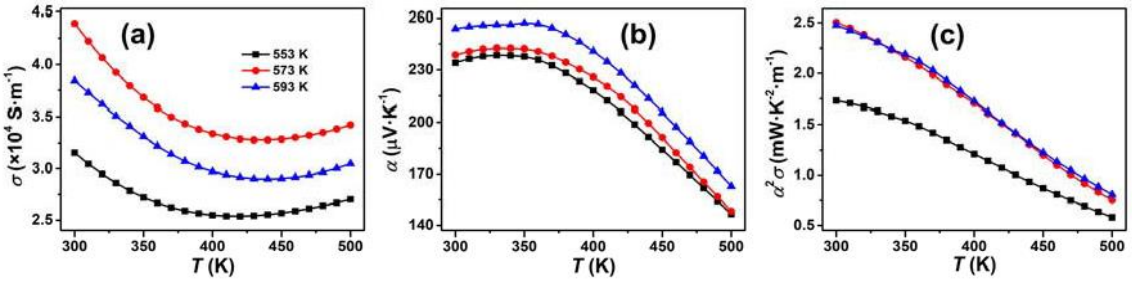

Supplementary Fig. 11 Electrical properties of MB-BST/EP films under different peak sintering temperature. Temperature dependence of (**a**) electrical conductivity, (**b**) Seebeck coefficient, and (**c**) *PF* of the MB-BST/EP films under different peak sintering temperature.

S6. Effect of heating rate during MB-SPS

The effect of heating rate during MB-SPS was investigated while keeping the same peak sintering temperature of 573 K, holding time of 10 min, and uniaxial pressure of 20 MPa. The temperature dependence of σ, α and $\alpha^2\sigma$ of MB-BST/EP films under different heating rates is shown in **SFig. 12a-c**, respectively. The σ gradually decreases as the heating rate increases. The maximum σ at 300 K for MB-BST/EP film under the heating rate of 6 K/min, increased by 2.6 times compared with that of MB-BST/EP film under the heating rate of 27 K/min. The remarkable decreases of the σ for the MB-BST/EP film are attributed to the layered BST particles cannot grow adequately induced by the rapidly increased heating rate.[36, 40] The magnitude of α of MB-BST/EP films under different heating rates is shown in **SFig. 12b**. Regardless of the temperature, the magnitude of α first gradually decreases as the heating rate increases. The decreases of the α for the MB-BST/EP film are attributed to the increases in the gap between the layered BST particles. The $\alpha^2\sigma$ values of all the MB-BST/EP films under different heating rates are calculated as shown in **SFig. 12c**. The $\alpha^2\sigma$ values decrease as the heating rate increases, and the $\alpha^2\sigma$ values of BST/EP films are similar under 6 K/min and 9 K/min. Therefore, the optimum heating rate for the MB-BST/EP films preparation is less than 9 K/min.

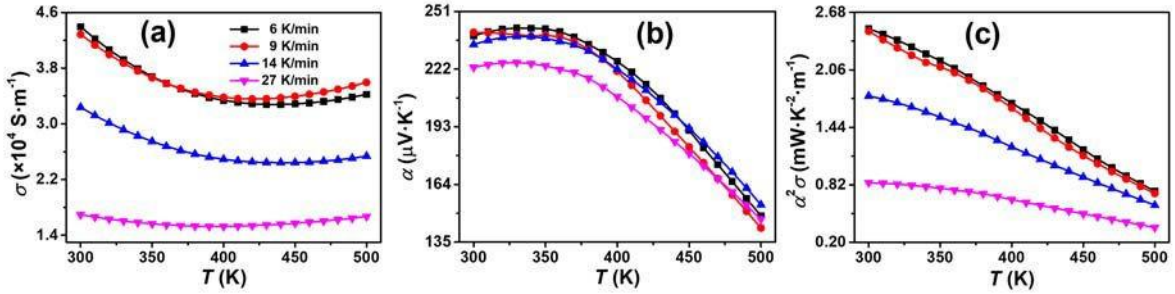

Supplementary Fig. 12 Electrical properties of MB-BST/EP films under different heating rates. Temperature dependence of (**a**) electrical conductivity, (**b**) Seebeck coefficient, and (**c**) *PF* of the MB-BST/EP films under different heating rates.

S7. Flexibility testing of MB-BST/EP film device

In this study, the polyimide (PI) substrate is flexible, and the PI substrate still has good flexibility after laser etching through-holes as shown in **SFig. 13a**. To test whether the MB-SPS method described in this study can prepare a strong oriented MB-BST/EP film with flexibility, we have evaluated the flexibility of the MB-BST/EP film device through testing the ratio of resistances (R/R_0) depending on bending radius and bending cycles by the flexible material and device testing system (FlexTest-TM-L) as shown in **SFig. 13b-c**. As shown in **SFig. 13b**, the internal resistance (R) was almost unchanged when the bending radius gradually decreased from 20 mm to 13 mm while it started to rapidly increase when the bending radius decreased from 13 mm to 10 mm. The TE leg was cracked when the bending radius was less than 13 mm. To further investigate the flexibility of the single-leg device, the R is measured during the cycling bending test under the condition of bending radius 13 mm. After 2000 bending cycles, the R only rises by about 8.68% as shown in **SFig. 13c**. These bending test results demonstrate the great application potential of flexible $Bi_{0.5}Sb_{1.5}Te_3$-based films. Therefore, the MB-SPS method described in this study can prepare a strong oriented MB-BST/EP film with flexibility.

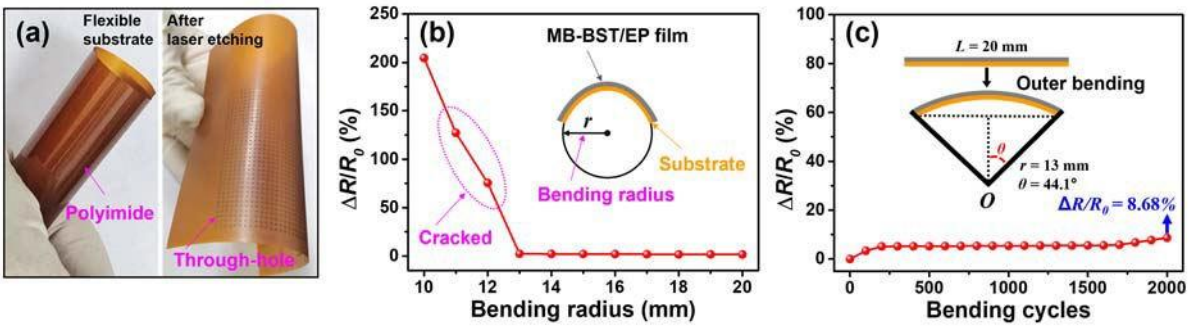

Supplementary Fig. 13 Flexibility of PI substrate and MB-BST/EP film device. (**a**) Photographs of the flexible PI substrate, (**b**) R/R_0 dependent bending radius, (**c**) R/R_0 dependent bending cycles.

References

1 F. K. Lotgering, *J. Inorg. Nucl. Chem.*, 1959, **9**, 113.

2 Y. Saberi, S. A. Sajjadi and H. Mansouri, *Ceram. Int.*, 2021, **47**, 11547-11559.

3 Z. Lin, C. Hollar, J. S. Kang, A. Yin, Y. Wang, H.-Y. Shiu, Y. Huang, Y. Hu, Y. Zhang and X. Duan, *Adv. Mater.*, 2017, **29**, 1606662.

4 D.-W. Ao, W.-D. Liu, Y.-X. Chen, M. Wei, B. Jabar, F. Li, X.-L. Shi, Z.-H. Zheng, G.-X. Liang, X.-H. Zhang, P. Fan and Z.-G. Chen, *Adv. Sci.*, 2022, **9**, 2103547.

5 M. Wei, X.-L. Shi, Z.-H. Zheng, F. Li, W.-D. Liu, L.-P. Xiang, Y.-S. Xie, Y.-X. Chen, J.-Y. Duan, H.-L. Ma, G.-X. Liang, X.-H. Zhang, P. Fan and Z.-G. Chen, *Adv. Funct. Mater.*, 2022, **32**, 2207903.

6 D. W. Newbrook, S. P. Richards, V. K. Greenacre, A. L. Hector, W. Levason, G. Reid, C. H. (Kees) de Groot (Kees) and R. Huang, *J. Alloy. Compd.*, 2020, **848**, 156523.

7 J. Andzane, A. Felsharuk, A. Sarakovskis, U. Malinovskis, E. Kauranens, M. Bechelany, K. A. Niherysh, I. V. Komissarov and D. Erts, *Mater. Today Energy*, 2021, **19**, 100587.

8 R. Eguchi, H. Yamamuro and M. Takashiri, *Thin Solid Films*, 2020, **714**, 138356.

9 Y. Sun, L. Qiu, L. Tang, H. Geng, H. Wang, F. Zhang, D. Huang, W. Xu, P. Yue, Y.-S. Guan, F. Jiao, Y. Sun, D. Tang, C.-A. Di, Y. Yi and D. Zhu, *Adv. Mater.*, 2016, **28**, 3351-3358.

10 N. V. Toan, T. T. K. Tuoi and T. Ono, *Energy Convers. Manage.*, 2020, **225**, 113442.

11 Y. Ding, Y. Qiu, K. Cai, Q. Yao, S. Chen, L. Chen and J. He, *Nat. Commun.*, 2019, **10**, 841.

12Q. Gao, W. Wang, Y. Lu, K. Cai, Y. Li, Z. Wang, M. Wu, C. Huang and J. He, *ACS Appl. Mater. Interfaces*, 2021, **13**, 14327-14333.

13C. Jiang, P. Wei, Y. Ding, K. Cai, L. Tong, Q. Gao, Y. Lu, W. Zhao and S. Chen, *Nano Energy*, 2021, **80**, 105488.

14 Y. Lu, Y. Qiu, K. Cai, Y. Ding, M. Wang, C. Jiang, Q. Yao, C. Huang, L. Chen and J. He, *Energy Environ. Sci.*, 2020, **13**,1240-1249.

15K. Ueda, Y. Yamada, T. Terao, K. Manabe, T. Hirai, Y. Asaumi, S. Fujii, S. Kawano, M. Muraoka and M. Murata, *J. Mater. Chem. A*, 2020, **8**, 12319-12322.

16Q. Jiang, H. Sun, D. Zhao, F. Zhang, D. Hu, F. Jiao, L. Qin, V. Linseis, S. Fabiano, X. Crispin, Y. Ma and Y. Cao, *Adv. Mater.*, 2020, **32**, 2002752.

17 D. Park, H. Ju and J. Kim, *J. Ind. Eng. Chem.*, 2021, **93**, 333-338.

18 H. Ju, D. Park and J. Kim, *J. Mater. Chem. A*, 2018, **6**, 5627-5634.

19Z. Lu, M. Layani, X. Zhao, L. P. Tan, T. Sun, S. Fan, Q. Yan, S. Magdassi and H. H. Hng, *Small*, 2014, **10**, 3551-3554.

20 W. Hou, X. Nie, W. Zhao, H. Zhou, X. Mu, W. Zhu and Q. Zhang, *Nano Energy*, 2018, **50**, 766-776.

21 C.-W. Chen and C.-N. Liao, *Mater. Chem. Phys.*, 2021, **259**, 124006.

22W. J. Parker, R. J. Jenkins, C. P. Butler and G. L. Abbott, *J. Appl. Phys.*, 1961, **32**, 1679-1684.

23 D. Maillet, S. André, J. C. Batsale, A. Degiovanni and C. Moyne. *John Wiley & Sons, Inc.*, 2000, 55-63.

24C. Dun, C. A. Hewitt, H. Huang, J. Xu, C. Zhou, W. Huang, Y. Cui, W. Zhou, Q. Jiang and D. L. Carroll, *Nano Energy*, 2015, **18**, 306.

25 W. S. Kim, G. Anoop, I. S. Jeong, H. J. Lee, H. B. Kim, S. H. Kim, G. W. Goo, H. Lee, H. J. Lee, C. Kim, J. H. Lee, B. S. Mun, J. W. Park, E. Lee and J. Y. Jo, *Nano Energy*, 2020, **67**, 104207.

26 S. Qu, C. Ming, P. Qiu, K. Xu, Q. Xu, Q. Yao, P. Lu, H. Zeng, X. Shi and L. Chen, *Energy Environ. Sci.*, 2021, **14**, 6586.

27 Y. Wang, S. M. Zhang and Y. Deng, *J. Mater. Chem. A*, 2016, **4**, 3554.

28 C. Liu, D. L. Shan, Z. H. Shen, G. K. Ren, W. Yue, Z. F. Zhou, J. Y. Li, D. Yi, J. L. Lan, L. Q. Chen, G. J. Snyder, Y. H. Lin and C. W. Nan, *Nano Energy*, 2021, **89**, 106380.

29 C. Wan, X. Gu, F. Dang, T. Itoh, Y. Wang, H. Sasaki, M. Kondo, K. Koga, K. Yabuki, G. J. Snyder, R. Yang and K. Koumoto, *Nat. Mater.*, 2015, **14**, 622.

30 Y. Lu, Y. Ding, Y. Qiu, K. Cai, Q. Yao, H. Song, L. Tong, J. He and L. Chen, *Acs Appl. Mater. Interfaces*, 2019, **11**, 12819.

31 L. Wang, Z. Zhang, L. Geng, T. Yuan, Y. Liu, J. Guo, L. Fang, J. Qiu and S. Wang, *Energy Environ. Sci.*, 2018, **11**, 1307.

32 L. Yang, M. P. Gordon, A. K. Menon, A. Bruefach, K. Haas, M. C. Scott, R. S. Prasher and J. J. Urban, *Sci. Adv.*, 2021, **7**, eabe6000.

33 L. Wang, Z. Zhang, Y. Liu, B. Wang, L. Fang, J. Qiu, K. Zhang and S. Wang, *Nat. Commun.*, 2018, **9**, 3817.

34 P. Banerjee, J. Huang, R. B. Ambade, E. Jang, M. Saeidi-Javash, Y. Zhang and D. Madan, *Nano Energy*, 2021, **89**, 106482.

35H. Qin, J. Zhu, N. Li, H. Wu, F. Guo, S. Sun, D. Qin, S. J. Pennycook, Q. Zhang, W. Cai and J. Sui, *Nano Energy*, 2020, **78**, 105228.

36R. D. Doherty, D. A. Hughes, F. J. Humphreys, J. J. Jonas, D. J. Jensen, M. E. Kassner, W. E. King, T. R. McNelley, H. J. McQueen and A. D. Rollett, *Mat. Sci. Eng. A*, 1997, **238**, 219.

37 R. D. Doherty, D. A. Hughes, F. J. Humphreys, J. J. Jonas, D. Juul Jensen, M. E. Kassner, W. E. King, T. R.

McNelley, H. J. McQueen and A. D. Rollett, *Mater. Today*, 1998, **1**, 14.

38 D. L. Medlin, N. Yang, C. D. Spataru, L. M. Hale and Y. Mishin, *Nat. Commun.*, 2019, **10**, 1820.

39 T. Zhu, L. Hu, X. Zhao and J. He, *Adv. Sci.*, 2016, **3**, 1600004.

40 R. Orrù, R. Licheri, A. M. Locci, A. Cincotti and G. Cao, *Mat. Sci. Eng. R*, 2009, **63**, 127.